JOURNAL OF GEOPHYSICAL RESEARCH, VOL. 105, NO. C8, PAGES 19,499–19,514, AUGUST 15, 2000

Sea surface velocities from sea surface temperature image sequences
1. Method and validation using primitive equation model output

Xavier Vigan,[1,2] Christine Provost,[3] Rainer Bleck,[4,5] and Philippe Courtier[3,6]

Abstract. An inverse variational finite element model is developed for the purpose of estimating ocean surface velocity fields from sequences of temperature fields. The cross-isotherm component of the velocity is controlled by a mixed layer integrated formulation of the heat balance. The aperture problem imposes additional constraints on the flow field: we control the divergence and the vorticity of the horizontal velocity. The method is then applied to sequences of sea surface temperature (SST) fields from a fine-mesh numerical simulation over the Brazil-Malvinas Confluence region. The difference between the actual velocity and the SST inverted velocity is 11% rms in magnitude and 17° rms in direction. These differences are analyzed; divergence and vorticity are computed. The hypothesis of neglecting the source terms made in the formulation of the mixed layer integrated heat balance is verified. The sensitivity of the solution to the influence of the constraints is examined. Perturbations are performed yielding fields of ellipses of covariance. We obtain on average 15% uncertainties in magnitude and 25° in direction of the velocity. Differences between the actual and SST inverted velocities fall into those covariance ellipses, except over regions where temperature does not change from one image to the other.

1. Introduction

The problem of estimating two-dimensional velocity fields from sequences of two-dimensional tracer fields is addressed. Sequences of sea surface temperature (SST) images provide a synoptic view of the surface of the ocean several times a day in the absence of cloud cover. One would like to estimate sea surface velocity fields suggested by the apparent motion of surface oceanic patterns observed on the image series. Previous efforts [*Vastano and Reid,* 1985; *Kelly,* 1989; *Kelly and Strub,* 1992; *Simpson and Gobat,* 1994] tend to infer sea surface velocities from sequences of advanced very high resolution radiometer (AVHRR) images. The problem has been approached in three ways: by subjective feature tracking (SFT) [*Vastano and Borders,* 1984; *Vastano and Reid,* 1985; *Vastano et al.,* 1985; *Svejkovsky,* 1988], by maximum cross correlation statistical methods (MCC) [*Emery et al.,* 1992; *Garcia and Robinson,* 1989; *Ninnis et al.,* 1986; *Kamachi,* 1989; *Kelly and Strub,* 1992; *Wahl and Simpson,* 1990; *Simpson and Gobat,* 1994; *Zavialov et al.,* 1998], and by inversion of the heat equation (INV) [*Kelly,* 1989; *Kelly and Strub,* 1992]. The latter is also known as the optical flow method, widely explored in the domain of pattern recognition (see *Nagel and Enkelmann* [1986] for a review). The SFT method has two fundamental drawbacks. The displacement vectors resulting from manual tracking are subjective, in the sense that there are no quantitative arguments to support the velocities obtained. In addition, regions over which velocities can be estimated are usually sparse. *Kelly and Strub* [1992] show that the MCC and the INV approaches yield equivalent results. The velocities estimated by both methods exhibit realistic circulation schemes. However, comparisons to concomitant *in situ* velocity measurements yield errors of the order of 50% in magnitude (underestimation) and of 50-60° in direction [*Kelly and Strub,* 1992; *Kelly,* 1994].

[1]Laboratoire d'Océanographie Physique, Muséum National d'Histoire Naturelle, Paris.

[2]Now at Laboratoire d'Océanography Dynamique et de Climatologie, Centre National d'Études Spatiales, Paris.

[3]Laboratoire d'Océanography Dynamique et de Climatologie, Centre National de la Recherche Scientifique, Paris.

[4]Rosentiel School of Marine and Atmospheric Sciences, University of Miami, Miami, Florida.

[5]Now at Los Alamos National Laboratory, Los Alamos, New Mexico.

[6]Now at Météo France, Paris.

Paper number 2000JC900027.
0148-0227/00/2000JC900027$09.00

We reexamine the inversion of the heat equation model using a finite element approach. The formulation does not depend upon any constraints on the spatial resolution of the discretization. Perturbations provide a way to produce error bars on the velocity estimates. We apply the method to SST fields produced by a three-dimensional primitive equation ocean circulation model (Miami Isopycnic Coordinate Oceanic Model (MICOM)). This allows us to check whether hypothesis are verified and to quantify carefully limitation due to the formulation.

2. Method

2.1. Mixed Layer Integrated Formulation of the Heat Balance

We consider that temperature variations at the surface of the ocean are due to four processes: horizontal advection, upwelling, surface heat fluxes, and horizontal diffusion. The conservation of heat can be written as

$$\frac{\partial T}{\partial t}+u\frac{\partial T}{\partial x}+v\frac{\partial T}{\partial y}+w\frac{\partial T}{\partial z}=\kappa\nabla^2 T-\frac{\partial}{\partial z}\overline{w^t T^t}+\frac{1}{\rho_0 C_p}\frac{\partial q}{\partial z}, \tag{1}$$

where T is temperature, (u, v, w) is the velocity, κ is a coefficient of horizontal diffusion, superscript t represents turbulent fluctuations, ρ_0 is the average density of seawater, C_p is the specific heat of seawater, and q is the vertical heat flux. If we consider the ocean to be well mixed from the surface to a depth h, vertical integration of (1) between $-h$ and the surface yields

$$\frac{\partial T}{\partial t}+u\frac{\partial T}{\partial x}+v\frac{\partial T}{\partial y}=\kappa\nabla^2 T+\frac{Q}{h\rho_0 C_p}-\frac{\Delta T w_e}{h}, \tag{2}$$

where (u, v) are functions of horizontal coordinates, Q is the net heat flux at the surface, ΔT is the temperature difference between the mixed layer and the water below, and w_e is the entrainment velocity at the base of the mixed layer.

For the purpose of estimating bidimensional velocity fields we use pairs of temperature fields separated by a time step δt. In (2), horizontal temperature gradients are computed from the mean of the temperature fields [*Walker*, 1994; *Nagel and Enkelmann*, 1986]. The temporal derivative of temperature can be approximated by a first-order Taylor expansion $\delta T(x, y)/\delta t$. Following *Wahl and Simpson* [1990], horizontal diffusion can be neglected if the time step between successive fields is short enough (typically 12 hours) for eddy diffusion not to affect the temperature field significantly. The source terms $Q/(h\rho_0 C_p)$ and $(\Delta T w_e)/h$ are not known at high spatial resolution: they are represented by a single term S. Equation (2) thus becomes

$$\frac{\partial T}{\partial t}+u\frac{\partial T}{\partial x}+v\frac{\partial T}{\partial y}=S, \tag{3}$$

where $S = Q/(h\rho_0 C_p) - (\Delta T w_e)/h$. The relative contribution of entrainment and surface heat fluxes on the heat balance will be examined from the output of a primitive equation model in section 3.

2.2. Additional Constraints

The velocity (u, v) cannot be estimated from (3) alone because the velocity components are constrained by only one equation: this is the aperture problem [*Barron et al.*, 1992]. One has to include additional dynamical constraints on (u, v) to solve (3).

The term $\mathbf{u}\cdot\nabla T$ vanishes for velocity vectors parallel to isotherms as well as for regions of zero gradients. In other words the along-isotherm component of the velocity lies in the null space of the equation as does any velocity where $\nabla T = 0$. *Kelly and Strub* [1992] use the horizontal divergence and the horizontal vorticity of (u, v) as regularizing constraints. From a physical point of view, if the divergence is small, the flow field to approaches quasi-geostrophy. Controling horizontal vorticity smoothes the resulting field. The cost function to be minimized reads

$$\mathcal{H}_1(u,v)=\left(\frac{\partial T}{\partial t}+\mathbf{u}\cdot\nabla T-S\right)^2+\alpha^2(\nabla\cdot\mathbf{u})^2+\beta^2(\nabla\times\mathbf{u})^2, \tag{4}$$

where α and β are penalty parameters introduced to tune the influence of the constraints on divergence and vorticity in the inversion [*Lawson and Hanson*, 1974; *Gill and Murray*, 1974]. The divergence- and vorticity-regularizing constraints have been discussed by *Amodei and Bendourhim* [1991] and are known as the divergence-curl vector splines. We use the Kelly and Strub [1992] model with a different numerical approach.

We examine a potential drawback of the choice of such constraints relative to the estimation of sea surface velocity fields. Consider solutions of the form

$$\mathbf{u}=\mathcal{F}(T)\mathbf{k}\times\nabla T, \tag{5}$$

where $\mathcal{F}$ is any bounded scalar function and $\mathbf{k}$ is the vertical unit vector. These solutions belong to the null space of $\mathbf{u}\cdot\nabla T$ since (5) is parallel to isotherms. They also belong to the null space of $\nabla\cdot\mathbf{u}$ because the divergence of the curl vanishes and the Jacobian of a function of T and T is zero. Since the curl of (5) is not zero, the minimization of the cost function (4) leads, by construction, to $\mathcal{F}(T) = 0$. Therefore solutions (equation (5)) are set to zero by the divergence-curl model. Notice that if $\mathcal{F} = (\beta g h)/(f\rho_0)$, where $\beta = -d\rho/dT$, g is gravity, h is the mixed layer depth, f is the Coriolis acceleration, and ρ_0 is the average density of seawater, (5) reduces to a vertically integrated formulation of the thermal wind relationship [*Kelly*, 1983]. From now on we shall refer

to (5) as the "thermal wind" solutions. The potential importance of that component of the flow will be assessed with primitive equation model output in section 4.

2.3. Numerical Procedure

The cost function (4) is solved with a finite element method (FEM) combined with a variational approach. The FEM is appropriate for dealing with minimization of quadratic functionals. A FEM method is based on the Galerkin approximation of the space over which equation (4) is defined [*Zienkiewicz*, 1977]. We approximate this space with quadratic triangular elements to allow the first derivatives of the velocity field to be defined. The calculus of variations and derivations are detailed in Appendix A.

3. Application to MICOM SST fields

3.1. High-Resolution MICOM Output

In this section we apply the inverse model presented in section 2 to temperature fields from the MICOM spanning the Brazil-Malvinas Confluence region. The output used stems from a run of the MICOM covering the world ocean [*Bleck et al.*, 1997] in which spatial resolution is $0.225° \times \cos(latitude)$. In the Brazil-Malvinas Confluence region the spatial resolution is 0.18° (~ 20 km). A 10 day temperature and velocity field sequence is used with a temporal resolution of 6 hours; it spans the beginning of austral fall, from January 25 to February 4. Fields of SST variations due to advection, entrainment, diffusion, surface heat fluxes, and convection are also available. The cold Malvinas Current (MC) water in the southwest of the area flows to the northeast along the continental shelf and the warm opposing Brazil Current (BC) water flows to the southwest (Plate 1). The two currents meet at ~ 39°S, which is a realistic position [e.g., *Olson et al.* 1988]. After meeting the BC the MC water returns to the south while the BC continues southward as far as 46°S. Coherent vortex patterns are observed to the east of the impact zone.

3.2. Strategy and Choice of a Solution

The domain is tessalated with second-order finite triangular elements. The quadratic finite element grid is generated using a Delaunay triangulation algorithm [*George*, 1992]. The resulting mesh (Plate 1a) comprises 2800 triangles the average sides of which measure 40 km. The distance between two adjacent nodes is 20 km.

A mapping of the SST fields onto the finite element mesh is necessary. In geophysical inverse problems the discretization is usually mapped onto the data, in the sense that the tracer is a model parameter [*Thacker*, 1989]. Here temperature is determined *a priori* for the sake of simplicity. For the purpose of mapping the data onto the mesh we make use of the finite element formulation to determine temperature T at each node through the minimization of

$$\mathcal{H}_2 = \left(\sum_{j=1}^{6} T_j \Phi_j - T_p \right)^2 \tag{6}$$

for each pixel p of the SST field. Performing variations on T_j of (6) yields a linear system of equations solved for T_j. Temperature variations $\partial T/\partial t$ are obtained by subtracting the first temperature field from the second. Horizontal temperature gradients are computed on the mesh at each node as

$$\begin{aligned} \frac{\partial T_j}{\partial x} &= \sum_{j=1}^{6} T_j \frac{\partial \Phi_j}{\partial x}, \\ \frac{\partial T_j}{\partial y} &= \sum_{j=1}^{6} T_j \frac{\partial \Phi_j}{\partial y}. \end{aligned} \tag{7}$$

For $[\alpha, \beta] \in \mathcal{R}^2$ an infinite number of solutions to (A3) and (A4) are obtained. One wants to isolate the one that most closely resembles the MICOM velocity field according to a given criterion. We evaluate the misfit to the heat balance as [*Kelly*, 1989]

$$\epsilon = \frac{\sum (\partial_t T + \mathbf{u} \cdot \nabla T - S)^2}{\sum (\partial_t T)^2}. \tag{8}$$

The misfit to the heat balance as a function of the weights imposed to divergence and vorticity (Figure 1a) reveals a minimum for ϵ associated with $\alpha = 0.95$ and $\beta = 2\ 10^{-3}$: that point corresponds to the best fit of the model to the data. The associated misfit on the heat balance is 14%. It is not zero because the constraints on divergence and vorticity overdetermine the problem in regions where the velocity is controlled by the heat balance (see Appendix B). The minimization of the total cost function (4) yields a compromise between the different constraints. None of them is satisfied exactly. The rms difference between the "real" velocity magnitude and the one estimated by the inverse model (Figure 1b) also exhibits a minimum. That area matches the minimum misfit region around $\alpha = 1.07$ and $\beta = 1.9 \times 10^{-3}$. The rms difference is 11% in magnitude and 17° in direction. The solution associated with the best fit of the model to the data is therefore a good candidate for a realistic flow field. The MICOM velocity field (Figure 2a) and the velocity field sought by the inverse model (Figure 2b) both present velocity magnitudes of $0.5 - 0.9$ m s^{-1} in the BC, of $0.4 - 0.6$ m s^{-1} in the MC, and ~ 1 m s^{-1} across eddies to the southeast of the confluence. The differences between both fields will be described in section 3.3.

3.3. Error Estimates and Ellipses of Covariance

Can this method yield error estimates? A natural approach in the context of inverse problems to estimate the error in the model parameters is to invert the Hes-

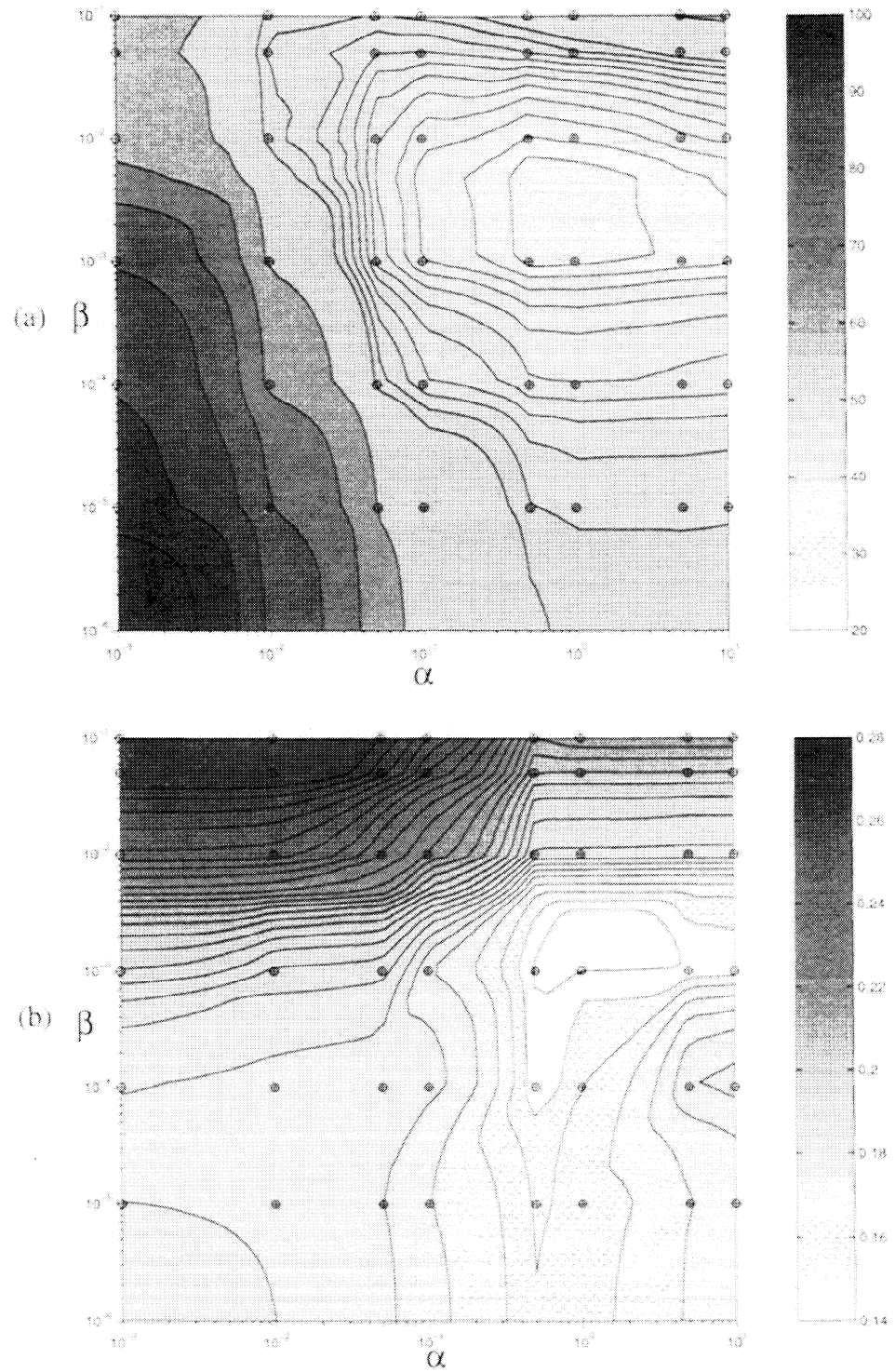

Figure 1. (a) Misfit to the heat balance (percent) as a function of the weight of the constraints on divergence α and on vorticity β. The misfit is minimum for $\alpha = 0.95$ and $\beta = 2\ 10^{-3}$. (b) The rms difference (m s^{-1}) between the MICOM velocity magnitude and the inverted velocity magnitude as a function of the weights of the constraints on divergence and vorticity. We observe a minimum around $\alpha = 1.05$ and $\beta = 1.9 \times 10^{-3}$.

sian matrix of the cost function [*Lorenc,* 1986; *Thacker,* 1989]. However, the number of model parameters involved here prevents the inversion of the Hessian matrix. For the purpose of estimating an error, another approach is to perform a sensitivity study of the solution to the influence of the constraints. If we vary α and β in (A3) and (A4) and restrain solutions whose misfit lie below a given level, we are left with a family

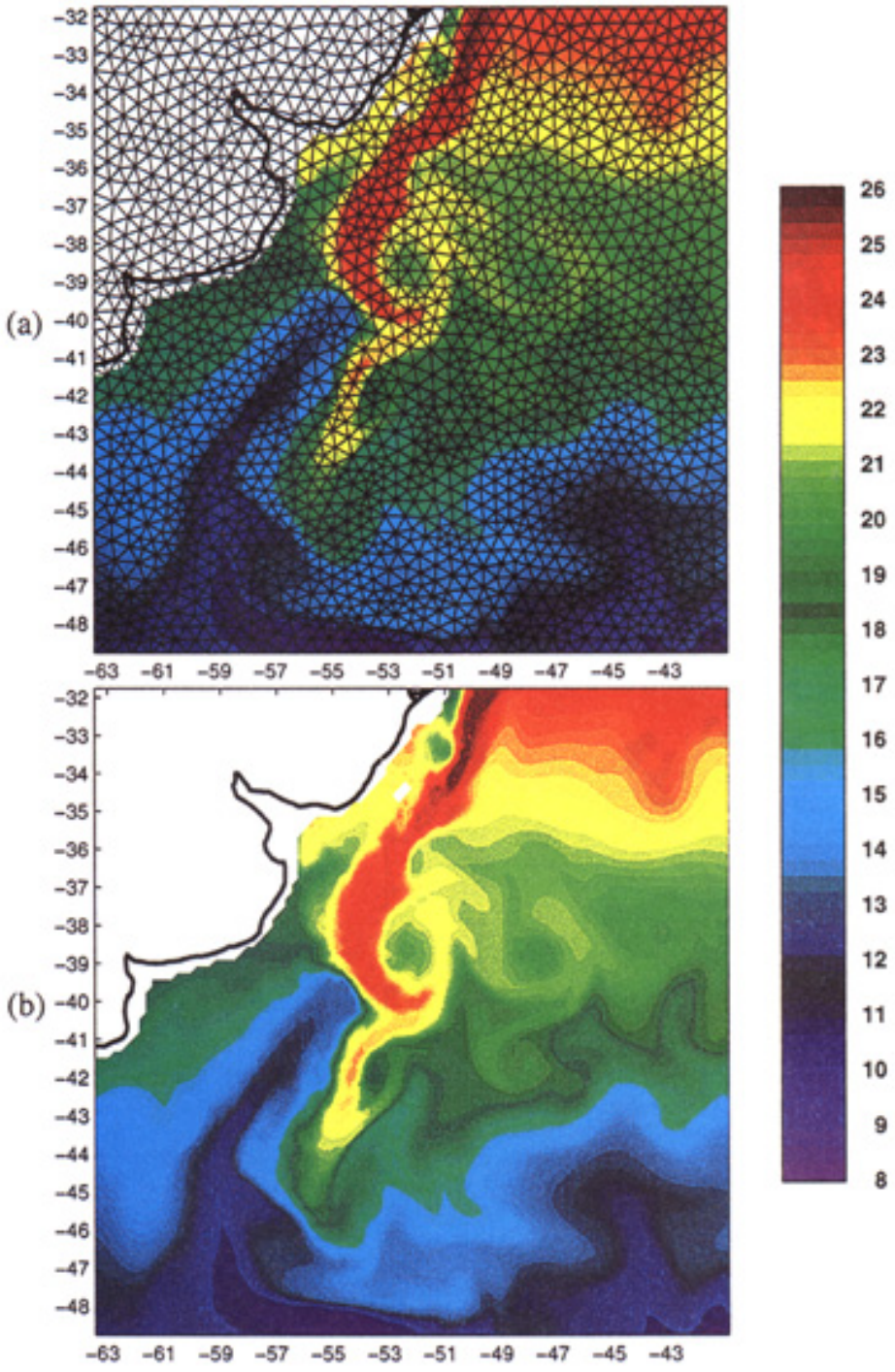

Plate 1. Two temperature fields (degrees celsius) from a global Miami Isopycnic Coordinate Oceanic Model (MICOM) run for January 25 (a) at 0600 and (b) at 1800. The model is forced by monthly atmospheric climatology.

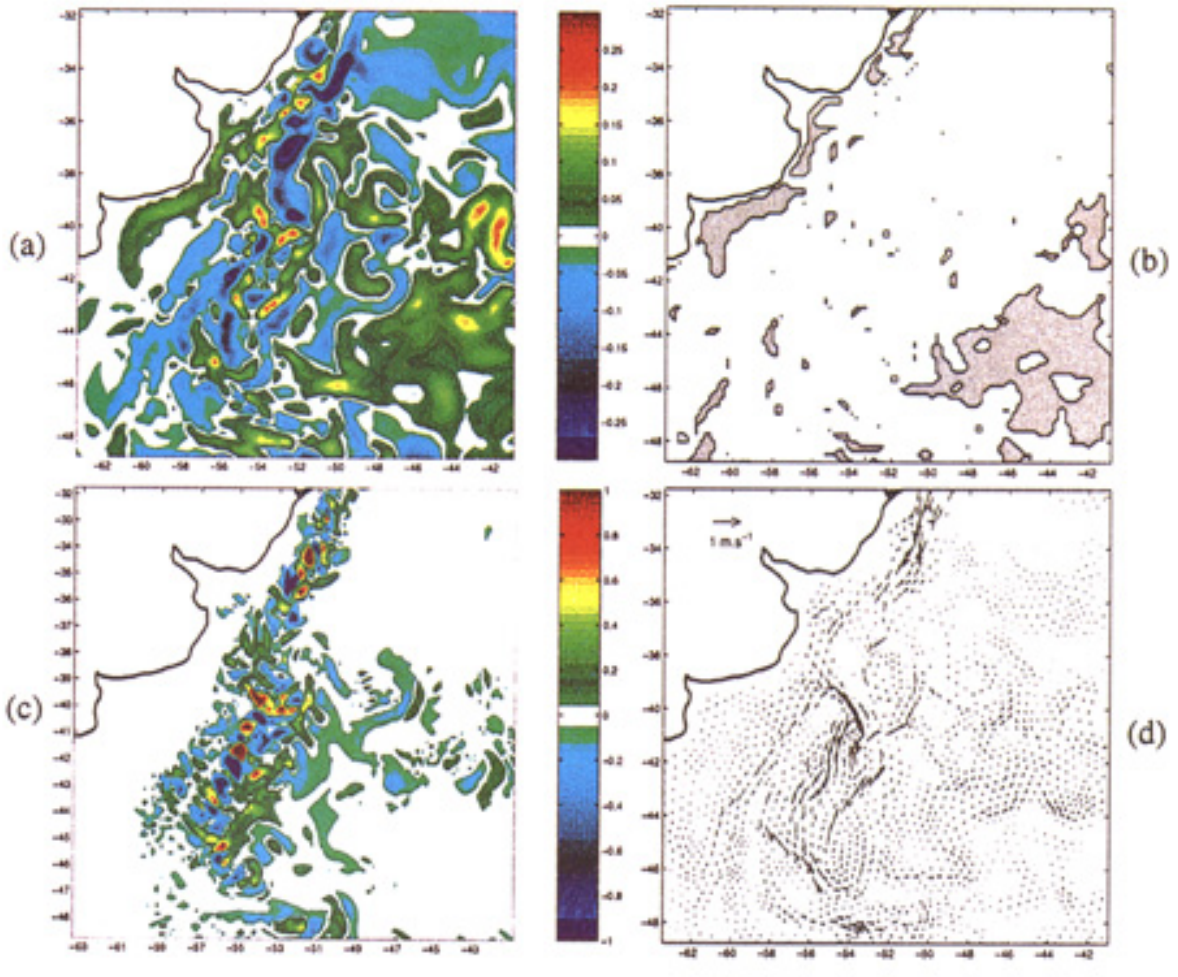

Plate 2. (a) Difference between the magnitude of the MICOM velocity field and the inverted velocity field (m s^{-1}). We observe differences of small spatial scale on the western boundary of the BC and over regions of strong horizontal temperature gradients around 40°S. Differences of the order of 0.2 m s^{-1} are found to the east of the region at 40°S and to the southeast between 42° – 48°S. (b) Difference between the error estimated on the magnitude of the velocity and Plate 2a. Gray (white) regions correspond to an underestimation (overestimation) of the error. (c) Temporal derivative of temperature $(^{\circ}C(12\,hours)^{-1})$. We observe a strong variability along the BC in the impact zone and in the BC overshoot. The variability is close to zero to the southeast, to the northeast and on the continental shelf. (d) The thermal wind velocity field obtained by a least squares fit of $\mathcal{F}(T)\mathbf{k} \times \nabla T$ to the MICOM velocity. Energetic areas can be observed in the BC overshoot and to the north of the BC.

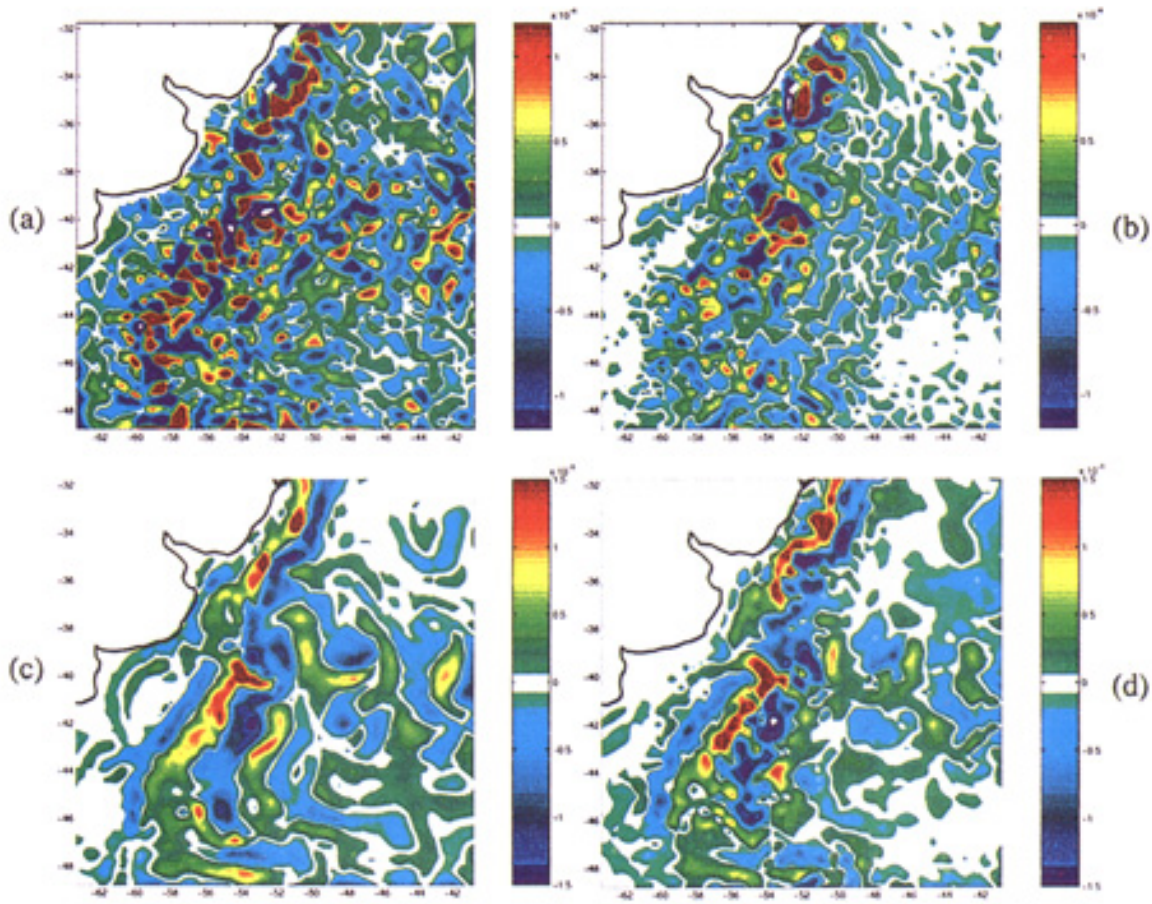

Plate 3. (a) Divergence of the MICOM velocity (s^{-1}). (b) Divergence of the inverted velocity (s^{-1}). (c) Vorticity of the MICOM velocity (s^{-1}). (d) Vorticity of the inverted velocity (s^{-1}).

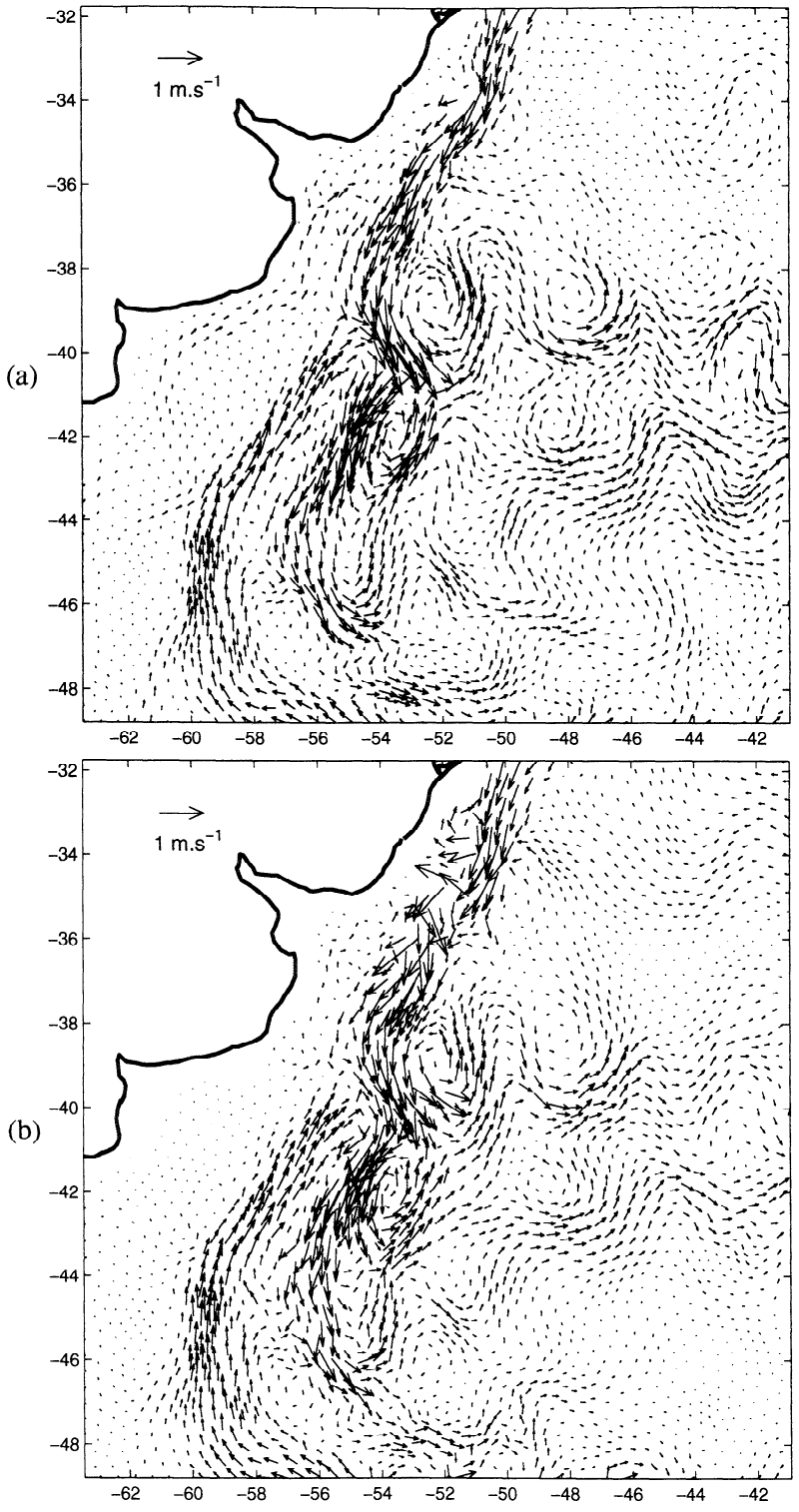

Figure 2. (a) MICOM velocity field mapped onto the finite element mesh. Magnitudes vary from 0.5 to 0.9 $m\,s^{-1}$ in the BC, vary from 0.4 to 0.6 $m\,s^{-1}$ in the MC, and are $\sim 1\,m\,s^{-1}$ across the eddies east of the confluence. (b) Velocity field estimated by the inverse model.

of "acceptable" solutions. In order to set a threshold on the misfit to the heat balance, we examine the relative contribution of heat fluxes, entrainment, and diffusion to the heat budget. In effect, we assumed that the MICOM fields used here are "perfect," in the sense that they are not subject to the influence of the source terms. Unmodeled processes can yield errors in the velocity estimates. We define the quantity

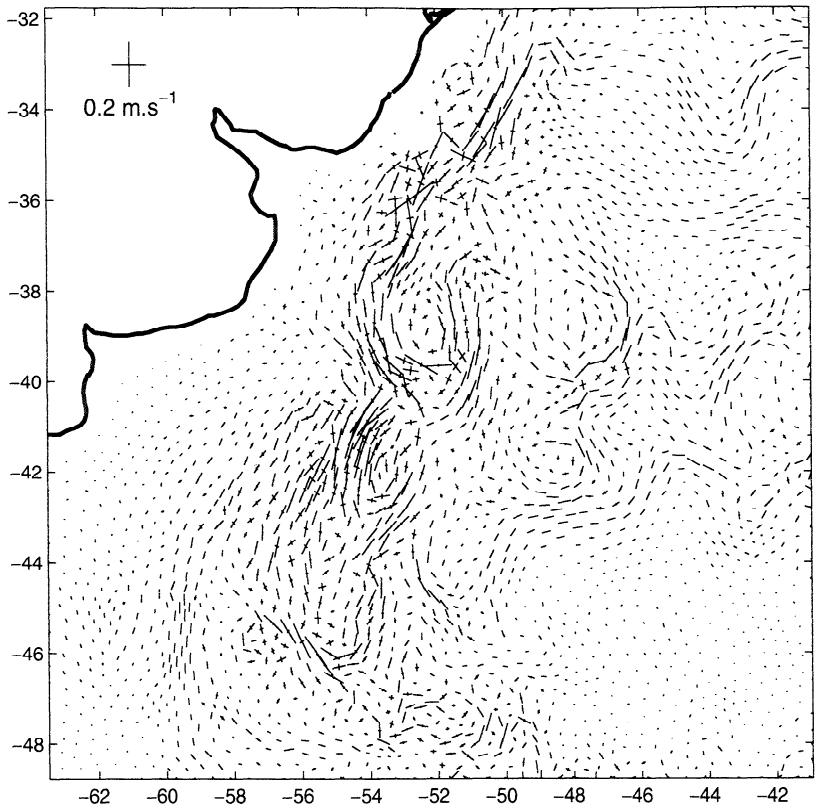

Figure 3. Ellipses of covariance field computed from a family of 14 velocity fields estimated through perturbations of the influence of the constraints on the solution under a misfit level of 24%. The ellipses provide an estimate of the error of the velocity. The rms value is 15% for the magnitude relative to the velocity and 25° for the direction.

$$\epsilon' = \frac{\sum \left\{ \partial_t T - (\Delta T w_e)/h - \kappa \nabla^2 T - Q/(h\rho_0 C_p) \right\}}{\sum \{\partial_t T\}}. \tag{9}$$

In a manner analoguous to (8), (9) relates the contribution of the source terms to temperature variations. We obtain 16%. Therefore a realistic misfit level of 16% greater than the minimum misfit is chosen to select a family of acceptable solutions and determine an error field. We are left with 18 velocity fields among 64. We compute variances and covariances on both components of the velocity to yield a field of ellipses of covariance [*Brandt*, 1976] (Figure 3). These ellipses provide a graphical representation of an estimate of the error of the solution. The uncertainty of the magnitude of the velocity is defined as the standard deviation of the magnitude of the velocity vector distribution used to compute the ellipses of covariance: we obtain a rms value relative to the average velocity of the distribution of 15%. We define an estimate of the error in the direction as the standard deviation of the direction of the velocity vector distribution used to compute the ellipses of covariance: the resulting rms value is 25°.

What can we learn from these estimates of the error? The orientation of the larger axis is parallel to isotherms. The smaller axis is much smaller than the greater. The sensitivity of the solution is important in a direction parallel to isotherms. In effect, while the cross-isotherm component of the velocity is controlled by the data, the component parallel to isotherms is controlled by the regularizing constraints.

4. Discussion

In section 2 we made some hypotheses on the source terms. We neglected diffusion, entrainment, and heat fluxes and accounted for their possible influence on the heat balance in section 3 by setting a threshold on the misfit for computing error bars. The rms difference between the MICOM velocity and the one sought by the inversion falls within the error bars. That result tends to show that neglecting the source terms in the inversion is a realistic hypothesis once their contribution is taken into account in the error estimates. However, one must examine wether that hypothesis is verified spatially or not. The misfit to the heat balance (Figure 4a) is not zero over regions of strong temperature gradients and to the east and southeast of the region. Advection over those regions is not the only significant process and must be balanced by the source terms. In effect, to the southeast, for example, as $\partial T/\partial t$ is zero, advection is negative, and the sum of the source terms is positive

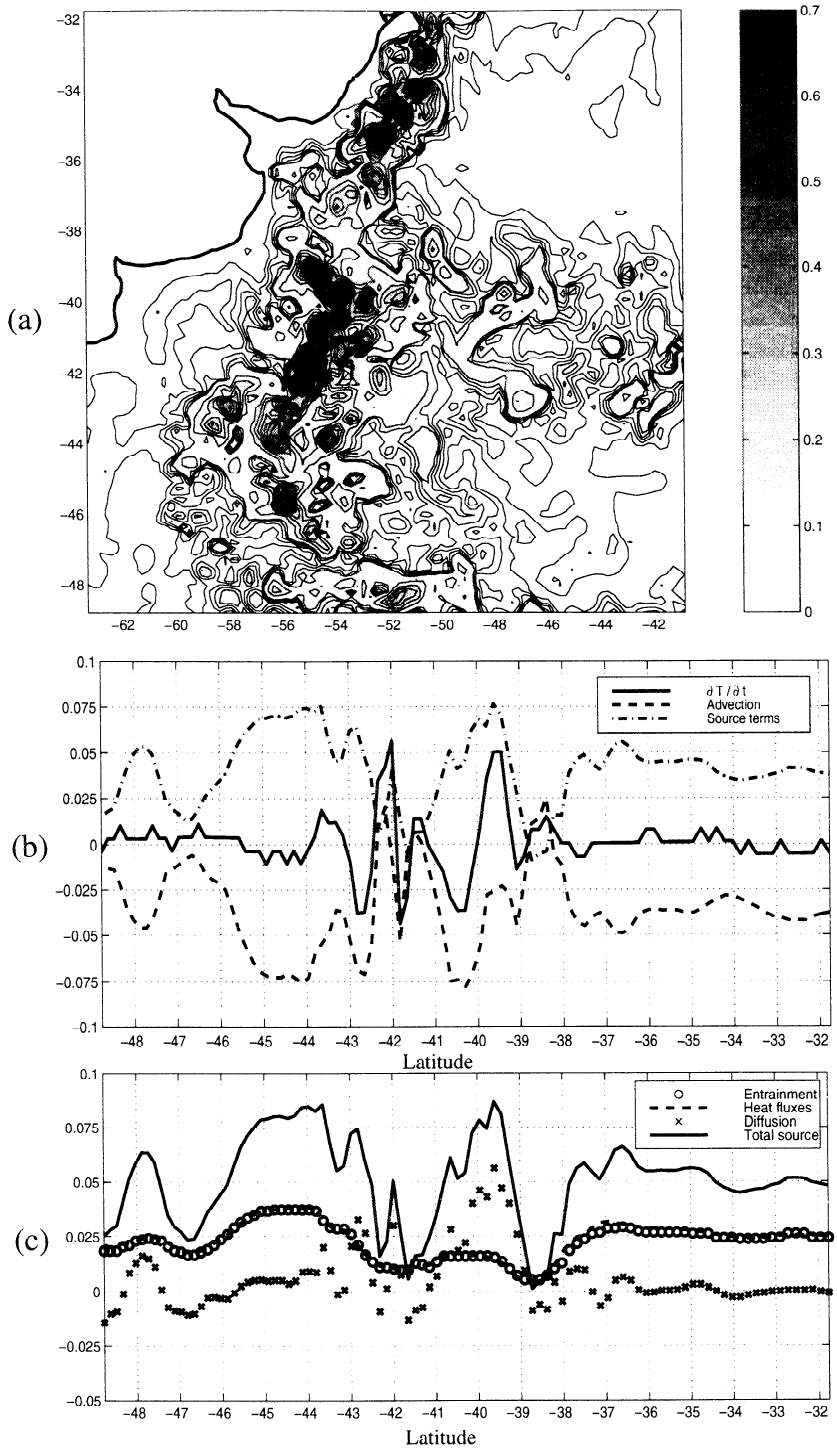

Figure 4. (a) Absolute value of the misfit to the heat balance (°C (12hours)$^{-1}$). (b) Temperature variation (solid line), advection (dashed line) and sum of the source terms (dash-dotted line) along 45.7°W (°C (12hours)$^{-1}$). (c) Contribution (°C (12hours)$^{-1}$) of entrainment (circles), surface heat fluxes (dashed line) and diffusion (crosses) to the source terms (solid line) along 45.7°W (entrainment and surface heat fluxes are in near balance).

(Figure 4b). Entrainment and surface heat fluxes (Figure 4c) seem to be the predominating processes over that area. The same observation can be made concerning the continental shelf and regions of strong temperature gradients in the impact zone.

In order to determine the possible failures of the error estimates we identify regions over which these errors are lower than the absolute value of the difference between the "true" and the inverted field (Plate 2a). The estimation of the error fails over three regions (Plate

2b): to the southeast between 42° and 48°S, 50° and 41°W, to the east of the Confluence around 40°S, and on the continental shelf. These underestimates are due to the fact that over those regions, temperature variations are zero: the velocity estimated by the inverse model is therefore zero, and the ellipses sought by the sensitivity study are very small.

We noticed in section 1 that a family of solutions are forced to zero by the inverse model. These solutions have the form $\mathbf{u}_{TW} = \mathcal{F}(T)\,\mathbf{k} \times \nabla T$ where TW is thermal wind. To estimate the possible contribution of such solutions to the differences between the MICOM and the inverted fields and to the underestimates of the error, we fit $\mathbf{u}_{INV} + \mathcal{F}(T)\,\mathbf{k} \times \nabla T$ (where $\mathbf{u}_{INV}$ is the solution to the inversion) to the MICOM velocity field. The problem is one of determining the function $\mathcal{F}$. We expand $\mathcal{F}$ on a Legendre polynomial basis and minimize the functional

$$\mathcal{H}_3 = \left[u_{MICOM} - u_{INV} + \mathcal{F}(T)\,\frac{\partial T}{\partial y}\right]^2 + \left[v_{MICOM} - v_{INV} - \mathcal{F}(T)\,\frac{\partial T}{\partial x}\right]^2 \qquad (10)$$

with

$$\mathcal{F}(T) = \sum_{n=0}^{N} a_n P_n(T), \qquad (11)$$

where $P_n(T)$ are the Legendre polynomials and a_n are the parameters of the fit. We use $N = 5$ because expending to higher orders does not yield significantly different results. The rms difference between the magnitude of $\mathbf{u}_{MICOM}$ and $\mathbf{u}_{INV} + \mathbf{u}_{TW}$ is now 6%. The southeast, the northeast and the continental shelf are regions characterized by a very weak spatiotemporal variability from one field to the other (Figure 2c). These areas match fairly well the ones for which the error in the field of ellipses of covariance is underestimated. To the southeast, when $\partial T/\partial t$ is zero, the magnitude of horizontal temperature gradients (not shown) is not zero, and the MICOM velocity is not zero either. To the northeast, $\partial T/\partial t$, temperature gradients, and the MICOM velocity are all zero. On the continental shelf, when $\partial T/\partial t$ and temperature gradients are zero, the velocity is not. The estimate of the error to the northeast is good because the true velocity is zero: the inverse model estimates a zero velocity because $\partial T/\partial t$ is zero. However, to the southeast the inverse model estimates a zero velocity also because $\partial T/\partial t = 0$, but the true velocity is not zero. That situation highlights the fact that the inverse model sets the thermal wind solutions (Figure 2d) to zero.

Another possible reason for why the velocity magnitudes have been underestimated in previous efforts is that the grid resolution was too coarse. *Kelly* [1989] developed an argument based on the Courant-Friedrichs-Lewy (CFL) condition relative to the inverse model to determine a realistic mesh size. The CFL criterion requires the mesh size δx to be greater than the velocity u times the time step between images δt. Our inversions do not depend upon the CFL criterion. In effect, the best magnitude (Figure 5a) and phase (Figure 5b) of the complex correlation between the MICOM velocity field and the inverted one are obtained for a finite element grid resolution of 20-40 km (the resolution of the MICOM grid is $\sim$ 20 km in the area). Since the time step between the first and second temperature field is 12 hours and since the maximum cross-isotherm velocity in the MICOM fields is 0.6 m s^{-1}, the CFL criterion imposes a grid resolution of 52 km. However, with the inverse model presented here the best estimates of the velocity are obtained for a grid size close to the MICOM one. These results do not yield conclusions about the CFL issue. We solely observe that the inverse model presented here yields the most significant estimates of the velocity when the grid resolution is close to the spatial resolution of the MICOM.

In order to go further in the analysis of the results we examine-higher order quantities, such as the divergence and vorticity of the horizontal velocity fields. We compute both terms at each node of the mesh using the finite element formulation and remap them onto the MICOM grid. The order of magnitude of the divergence of the MICOM velocity (Plate 3a) and of the inverted velocity (Plate 3b) is 10^{-6}s^{-1}. The order of magnitude of vorticity (Plates 3c and 3d) is 10^{-5}s^{-1} for both fields. These values are realistic even though nothing *a priori* in the method prescribes these orders of magnitude. The divergence field exhibits smaller spatial scales than the vorticity. The comparison along 39°S of the divergence (Figure 6a) and vorticity (Figure 6b) fields computed from the MICOM velocity and from the inverted one yields a better estimate of vorticity (25% error rms) than divergence (35% error rms).

5. Conclusions

The problem of estimating absolute velocities from the apparent motion of oceanic temperature patterns lies in the estimation of the along-isotherm component of the velocity. Regularizing constraints on the solution must be taken into account in order, on the one hand, for the problem to be wellposed and on the other hand, to add *a priori* missing physics to the flow field. We control the horizontal divergence and vorticity and notice that thermal wind-type solutions are forced to zero by the model. The solutions estimated by inversion are realistic in comparison with the MICOM fields, except over regions of zero temporal variability of temperature and of strong horizontal temperature gradients as well as on the coastal boundary. An examination of the con-

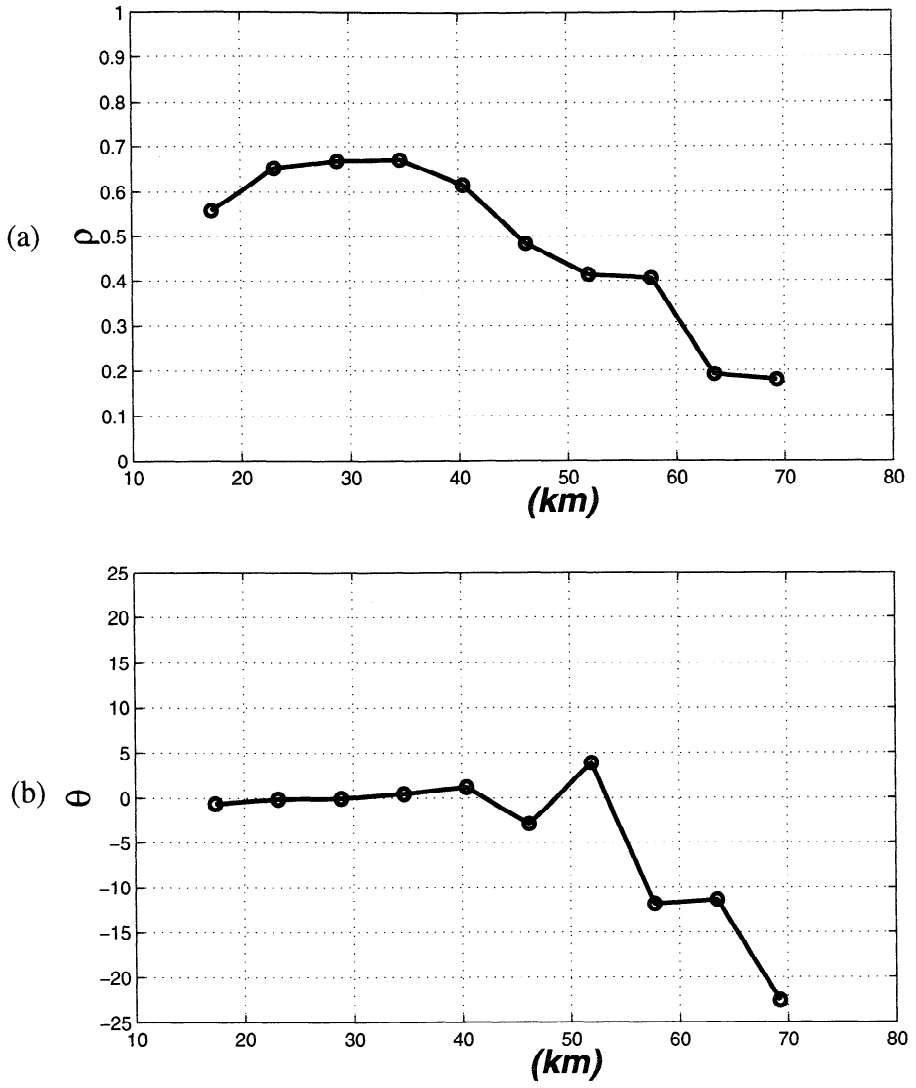

Figure 5. Complex correlation between the MICOM velocity field and the inverted velocity. (a) Magnitude (normalized) of the correlation as a function of the average triangle side of the finite element mesh. (b) Phase (degrees) of the correlation. The best results are obtained for a triangle side of 20-40 km. The solution selected for each triangle side corresponds to the best fit of the inverse model to the data.

tribution of the source terms over those regions shows that errors in the estimated velocity field can be explained by the fact that these terms are neglected. A sensitivity study of the solution to perturbations of the weight of the constraints yields a field of ellipses of covariance providing an estimate of the error. The ellipses present a larger axis with a mainly along-isotherm orientation, illustrating the fact that the constraints on divergence and vorticity control that component of the solution. Regions over which the error estimates fail correspond to zero temperature variations and to a significant contribution of the source terms, especially of surface heat fluxes and entrainment. An analysis of the contribution of the thermal wind solutions to the error shows that they also explain part of it. Moreover, the fact that these solutions are set to zero leads to an underestimation of the error over areas where the temporal derivative of temperature is zero and where the velocity is not zero. We believe that the fact that the thermal wind solutions are forced to zero could explain part of the underestimation of the velocity magnitudes obtained by *Kelly* [1989], *Kelly and Strub* [1992], and *Kelly* [1994], especially across jets and energetic patterns where horizontal temperature gradients are strong but the time derivative of temperature is not. Errors on the velocity magnitude may arise in the inversions because these solutions are forced to zero. Moreover, our study indicates that the best velocity estimates are obtained when the grid resolution is close to the MICOM resolution. As the problem is formulated here, the grid resolution appears to be a sensitive parameter relative to the velocity estimates.

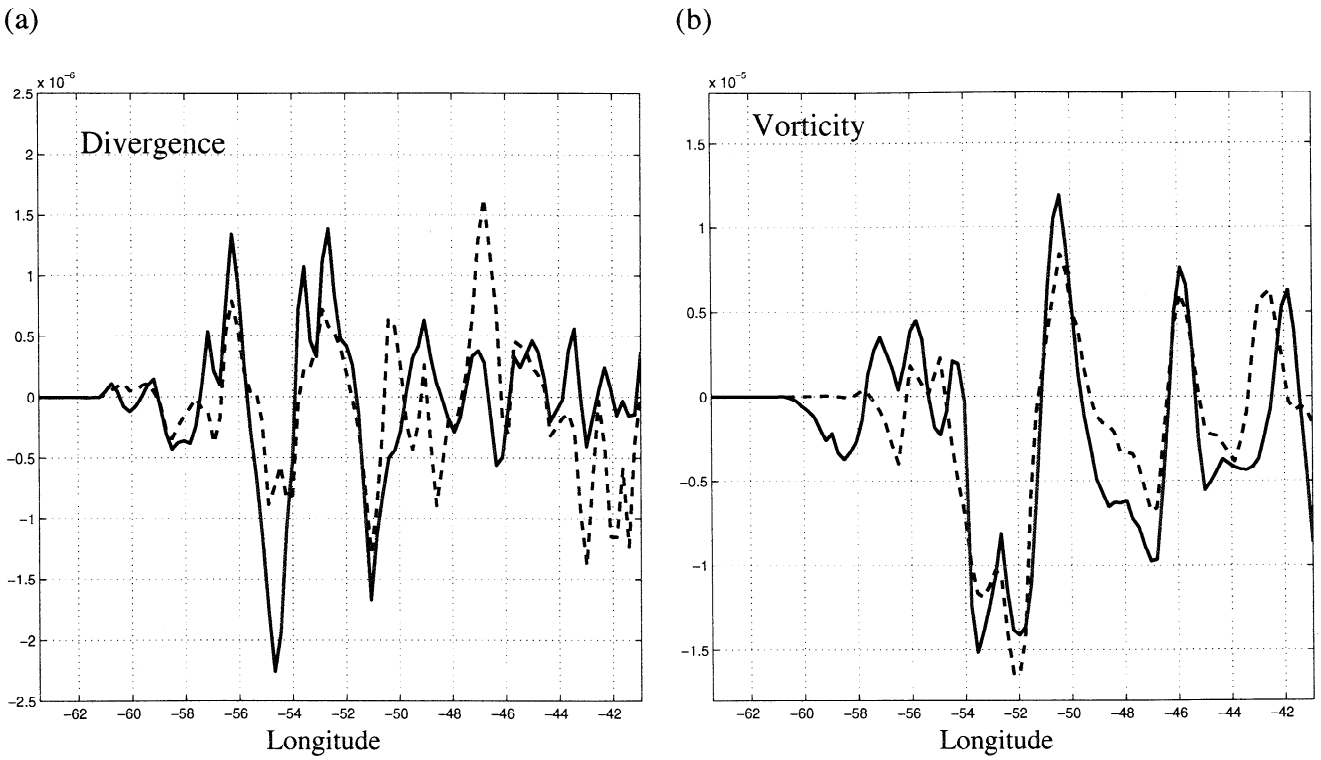

Figure 6. Comparison of the divergence and vorticity of the horizontal velocity stemming from the MICOM and from the inversion. (a) Divergence along 39°S from MICOM (solid line) and from the inversion (dashed line). The order of magnitude is $10^{-6}s^{-1}$, and the rms error is 35%. (b) Vorticity along 39°S from MICOM (solid line) and from the inversion (dashed line). The order of magnitude is $10^{-5}s^{-1}$, and the rms error is 25%.

Overall, the velocity estimates and the associated error fields should be interpreted with care over regions where $\partial T/\partial t$ is zero, especially on the boundaries or near the coastline of the fields. That observation is specific to the results sought from the MICOM fields. As shown by Vigan et al. [this issue], temporal temperature variations observed on AVHRR SST images present a better spatial distribution than they do over the MICOM fields. That is due to the fact that small-scale oceanic surface patterns observed on the SST images leave a signature on temporal temperature variations.

Appendix A: Finite Elements and Variational Calculus

Considering a set of basis functions Φ_j defined over each element, the velocity (u, v) can be expended as

$$\begin{cases} u(x,y) = \sum_{j=1}^{6} U_j \Phi_j(x,y) \\ v(x,y) = \sum_{j=1}^{6} V_j \Phi_j(x,y) \end{cases} \quad \text{(A1)}$$

where j denotes the nodes of a given triangle and (U_j, V_j) is the velocity at these nodes. Note that the summation is over $j = 1 - 6$ because the quadratic triangular elements require six nodes to be defined (Figure A1).

Substituting (A1) into (4) yields

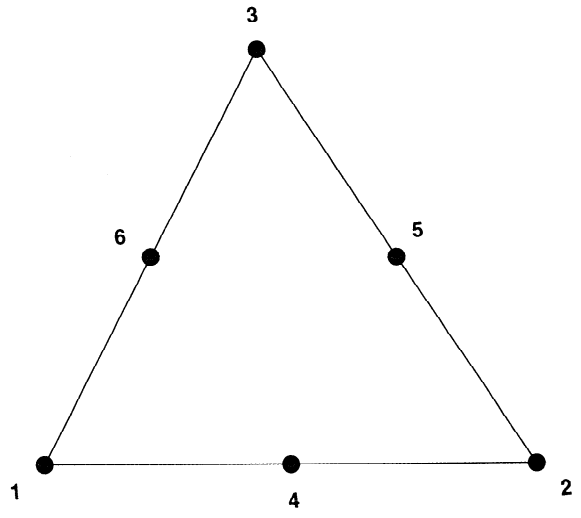

Figure A1. Quadratic finite element. The numbers represent the nodes defining the triangle.

$$\mathcal{H}_1(u,v) = \left[\begin{array}{l} \dfrac{T_i^{n+1} - T_i^n}{\delta t} - S_i \\ + \displaystyle\sum_j U_j \Phi_j \left(\frac{\partial T}{\partial x}\right)_i + \sum_j V_j \Phi_j \left(\frac{\partial T}{\partial y}\right)_i \end{array} \right]^2 + \alpha^2 \left(\sum_j U_j \frac{\partial \Phi_j}{\partial x} + \sum_j V_j \frac{\partial \Phi_j}{\partial y} \right)^2 + \beta^2 \left(- \sum_j U_j \frac{\partial \Phi_j}{\partial y} + \sum_j V_j \frac{\partial \Phi_j}{\partial x} \right)^2 \tag{A2}$$

for every node i. Variations on U_i and V_i of (A2) lead to the associated Euler-Lagrange equations of the problem

$$\sum_{i \in \Delta} \left\{ \begin{array}{l} \displaystyle\sum_j U_j \iint_\Omega \Phi_i \Phi_j \left(\frac{\partial T}{\partial x}\right)_i \left(\frac{\partial T}{\partial x}\right)_j \\ + \displaystyle\sum_j V_j \iint_\Omega \Phi_i \Phi_j \left(\frac{\partial T}{\partial x}\right)_i \left(\frac{\partial T}{\partial y}\right)_j \\ + \alpha^2 \left[\begin{array}{l} \displaystyle\sum_j U_i \iint_\Omega \frac{\partial \Phi_i}{\partial x} \frac{\partial \Phi_j}{\partial x} \\ + \displaystyle\sum_j V_i \iint_\Omega \frac{\partial \Phi_i}{\partial x} \frac{\partial \Phi_j}{\partial y} \end{array} \right] \\ + \beta^2 \left[\begin{array}{l} \displaystyle\sum_j U_i \iint_\Omega \frac{\partial \Phi_i}{\partial y} \frac{\partial \Phi_j}{\partial y} \\ - \displaystyle\sum_j V_i \iint_\Omega \frac{\partial \Phi_i}{\partial y} \frac{\partial \Phi_j}{\partial x} \end{array} \right] \end{array} \right\} = - \sum_{i \in \Delta} \left\{ \iint_\Omega \Phi_i \left(\frac{T_i^{n+1} - T_i^n}{\delta t} - S_i \right) \left(\frac{\partial T}{\partial x}\right)_i \right\} \tag{A3}$$

$$\sum_{i \in \Delta} \left\{ \begin{array}{l} \displaystyle\sum_j U_j \iint_\Omega \Phi_i \Phi_j \left(\frac{\partial T}{\partial y}\right)_i \left(\frac{\partial T}{\partial x}\right)_j \\ + \displaystyle\sum_j V_j \iint_\Omega \Phi_i \Phi_j \left(\frac{\partial T}{\partial y}\right)_i \left(\frac{\partial T}{\partial y}\right)_j \\ + \alpha^2 \left[\begin{array}{l} \displaystyle\sum_j U_i \iint_\Omega \frac{\partial \Phi_i}{\partial y} \frac{\partial \Phi_j}{\partial x} \\ + \displaystyle\sum_j V_i \iint_\Omega \frac{\partial \Phi_i}{\partial y} \frac{\partial \Phi_j}{\partial y} \end{array} \right] \\ + \beta^2 \left[\begin{array}{l} - \displaystyle\sum_j U_i \iint_\Omega \frac{\partial \Phi_i}{\partial x} \frac{\partial \Phi_j}{\partial x} \\ + \displaystyle\sum_j V_i \iint_\Omega \frac{\partial \Phi_i}{\partial x} \frac{\partial \Phi_j}{\partial x} \end{array} \right] \end{array} \right\} = - \sum_{i \in \Delta} \left\{ \iint_\Omega \Phi_i \left(\frac{T_i^{n+1} - T_i^n}{\delta t} - S_i \right) \left(\frac{\partial T}{\partial y}\right)_i \right\} \tag{A4}$$

where Δ represents the triangles encompassing node i and Ω denotes one of these triangles. Equations (A3) and (A4) are solved with a conjugate gradient algorithm.

Appendix B: Conditioning of the Inverse Model

Two subareas of the MICOM temperature fields of Plate 1 spanning 36°-41°S and 56°-49°W are selected in order to examine the conditioning of the inverse model. That shorter region is tessalated with second-order finite elements encompassing 86 nodes. The three linear operators of divergence, vorticity, and heat balance are computed in matrix form with the formalism of finite elements as detailed by *Lapidus and Pinder* [1982]. We also compute the Hessian matrix of each quadratic form

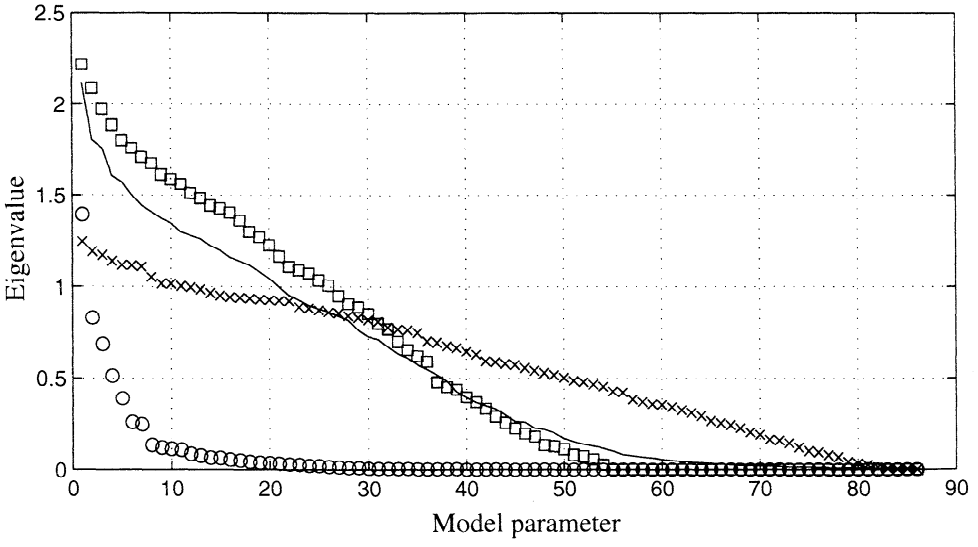

Figure B1. Eigenvalues of the Hessian matrices of the operators: heat balance (circles), divergence or vorticity (squares), sum of divergence and vorticity (crosses), and sum of the three operators (solid).

associated with the constraints. Analyzing the eigenvalues of the Hessian matrix of the cost function yields conclusions on the conditioning of the system [*Thacker*, 1989]. Figure B1 represents the eigenvalues of the Hessian matrices of the constraints. We observe that the hessian matrix associated with the heat balance comprises 43 nonzero eigenvalues, which is the dimension of its null space. The eigenvalues of the Hessian matrices of the divergence and vorticity operators are identical because divergence is the symmetrical part of the gradient operator and vorticity is the antisymetrical part. Among the eigenvalues, 38 are zero. We now examine the eigenvalues of the Hessian matrix of the sum of the divergence and vorticity operators: 78 are nonzero. The null space of the regularizing operator is therefore of dimension eight. It comprises the harmonical solutions for which $\nabla \cdot \mathbf{u} = 0$ and $\nabla \times \mathbf{u} = 0$ (nondivergent and nonrotationnal). The eigenvalues of the Hessian matrix of the sum of the three operators are all nonzero: the null space is empty, illustrating the fact that harmonical solutions are controlled by the data. In that example the largest eigenvalue is equal to 2, and the smallest one is 0.3×10^{-3}. Therefore, in terms of variance the best and the worst directions estimated differ by a factor of 10^{-4}; in terms of standard deviation both values differ by a factor 100.

In practice, the fact that the null space of the regularizing operator is not empty is not a problem. In effect we use a conjugate gradient algorithm to solve the linear system of equations stemming from the variational calculus. The search for the minimum is initialized with a flat velocity field: in this way the descending algorithm does not generate anything in the direction of the null space. In addition, these solutions (nondivergent and nonrotationnal) are not physically realistic, especially in the Brazil-Malvinas Confluence region: they correspond to a flow parallel to unidirectional isotherms. Even though the inverse model is not formally well posed, applications to realistic situations as the one described in section 3 are not subject to ill posedness.

References

Amodei, L., and M. N. Bendourhim, A vector spline approximation, *J. Approximation Theory, 67,* 51-79, 1991.

Barron, J. L., D. J. Fleet, S. S. Beauchemin, and T. A. Burkitt, Performance of optical flow techniques, *paper presented at IEEE Proceedings of Computer Vision and Pattern Recognition, Inst. of Electr. and Electr. Ing., New York,* 1992.

Bleck, R., S. Sun, and S. Dean, Global ocean simulations with an isopycnic coordinate model. In: Some new directions in science on computers, pp. 297-317, World Sci., River Edge, N.J., 1997.

Brandt, S., *Statistical and Computational Methods in Data Analysis,* 414 pp., North-Holland, New York, 1976.

Emery, W. J., C. Fowler, and C. A. Clayson, Satellite image derived Gulf Stream currents compared with numerical model results, *J. Atmos. Oceanic. Technolo., 9,* 286-304, 1992.

Garcia, C. A. E., and I. S. Robinson, Sea surface velocities in shallow seas extracted from sequential Coastal Zone Color Scanner satellite data, *J. Geophys. Res., 94,* 12,861-12,961, 1989.

George, P. L. *Automatic Mesh Generation: Application to Finite Element Methods,* John Wiley, New York, 1992.

Gill, P. E., and W. Murray, *Numerical Methods for Constrained Optimization,* 283 pp., Academic, San Diego, Calif., 1974.

Kamachi, M., Advective surface velocities from sequential images for rotational flow field: Limitations and applications of Maximum Cross Correlation Method with rotational registration, *J. Geophys. Res., 94,* 18,227-18,233, 1989.

Kelly, K. A., Swirls and plumes or application of statistical methods to satellite-derived sea surface temperatures, PhD. thesis, 210 pp., Scripps Inst. of Oceanogr., San Diego, California, 1983.

Kelly, K. A., An inverse model for near-suraface velocities from infrared images, *J. Phys. Oceanogr., 19,* 1845-1864, 1989.

Kelly, K. A., Reply, *J. Geophys. Res., 99,* 10,301, 1994.

Kelly, K. A., and P. T. Strub, Comparision of velocity estimates from advanced Very high resolution radiometer in the coastal transition zone, *J. Geophys. Res., 97,* 9653-9668, 1992.

Lapidus, L., and G. F. Pinder, *Numerical Solution of Partial Differential Equations in Science and Engineering,* 677 pp., John Wiley, New York, 1982.

Lawson, C. L., and R. J. Hanson, *Solving Least Squares Problems,* 340 pp., Prentice Hall, Englewood Cliffs, N. J., 1974.

Lorenc, A. C., Analysis methods for numerical weather prediction, *Q. J. R. Meteorol. Soc.,* , London, *112,* 1177-1194, 1986.

Nagel, H. H., and W. Enkelmann, An investigation of smoothness constraints for the estimation of displacement vector field from image sequences, *IEEE Trans. Pattern Analy. Mach. Intel., 8,* 565-593, 1986.

Ninnis, R. M., W. J. Emery, and M. J. Collins, Automated extraction of pack ice motion from advanced very high resolution radiometer imagery, *J. Geophys. Res., 91,* 10,725-10,734, 1986.

Olson, D., G. Podesta, R. H. Evans, and O. Brown, Temporal variations in the separation of Brazil and Malvinas Currents, *Deep Sea Res. Part I, 35,* 1971-1990, 1988.

Simpson, J. J., and J. I. Gobat, Robust velocity estimates, stream functions, and simulated lagrangian drifters from sequential spacecraft data, *IEEE Trans. Geosci. Remote Sens., 32,* 479-491, 1994.

Svejkovsky, J., Sea surface flow estimation from advanced very high resolution radiometer and Coastal Zone Color Scanner satellite imagery: A verification study, *J. Geophys. Res., 93,* 6735-6743, 1988.

Thacker, W. C., The role of the Hessian matrix in fitting models to measurements, *J. Geophys. Res., 94,* 6177-6196, 1989.

Vastano, A. C., and S. E. Borders, Sea surface motion over an anticyclonic eddy of the Oyashio front, *Remote Sens. Environ., 16,* 87-90, 1984.

Vastano, A. C., and R. O. Reid, Sea surface topography estimation with infrared satellite imagery, *J. Atmos. Oceanic Technol., 2,* 393-400, 1985.

Vastano, A. C., S. E. Borders, and R. E. Wittenberg, Sea surface flow estimation with infrared and visible imagery, *J. Atmos. Oceanic Technol., 2,* 401-408, 1985

Vigan, X., C. Provost, and G. Podesta, Sea surface velocities

from sea surface temperature image sequences. 2, Application to the Brazil-Malvinas confluence area, *J. Geophys. Res.*, this issue.

Wahl, D. D., and J. J. Simpson, Physical processes affecting the objective determination of near-surface velocities from satellite data, *J. Geophys. Res., 95,* 13,511-13,528, 1990.

Walker, S. J., Comment on "Comparison of velocity estimates from advanced very high resolution radiometer in the coastal transition zone" by K. A. Kelly and P. T. Strub, *J. Geophys. Res., 99,* 10,297-10,299, 1994.

Zavialov, P. O., R. D. Ghisolfi, and C. A. E. Garcia, An inverse model for seasonal circulation over the southern Brazilian Shelf: Near-surface velocity from the heat budget, *J. Phys. Oceanogr., 28,* 545-562, 1998.

Zienkiewicz, O. C., *The Finite Element Method,* 787 pp., McGraw-Hill, New York, 1977.

R. Bleck, Los Alamos National Laboratory, Los Alamos, NM 87545. (bleck@acl.lanl.gov)

P. Courtier, Météo France, 75007 Paris, France. (Philippe.Courtier@meteo.fr)

C. Provost and X. Vigan, Laboratoire d'Océanographie Dynamique et de Climatologie, 75005 Paris, France. (Xavier.Vigan@lodyc.jussieu.fr)

(Received May 28, 1999; revised January 12, 2000; accepted January 24, 2000.)